UC Berkeley
UC Berkeley Previously Published Works

Title

Nonadiabatic transition paths from quantum jump trajectories

Permalink

Journal

ISSN

Authors

Anderson, Michelle C
Schile, Addison J
Limmer, David T

Publication Date

DOI

Nonadiabatic transition paths from quantum jump trajectories ⊘

Michelle C. Anderson ⓘ ; Addison J. Schile; David T. Limmer ✉ ⓘ

Check for updates

CHORUS

CrossMark

View Online

Export Citation

12 February 2024 19:26:52

Nonadiabatic transition paths from quantum jump trajectories

View Online   Export Citation   CrossMark

Michelle C. Anderson,[1] (ID) Addison J. Schile,[1] and David T. Limmer[1,2,3,4,a] (ID)

AFFILIATIONS

[1] Department of Chemistry, University of California, Berkeley, California 94720, USA
[2] Kavli Energy NanoSciences Institute, University of California, Berkeley, California 94720, USA
[3] Chemical Sciences Division, Lawrence Berkeley National Laboratory, Berkeley, California 94720, USA
[4] Materials Sciences Division, Lawrence Berkeley National Laboratory, Berkeley, California 94720, USA

[a] Author to whom correspondence should be addressed: dlimmer@berkeley.edu

ABSTRACT

We present a means of studying rare reactive pathways in open quantum systems using transition path theory and ensembles of quantum jump trajectories. This approach allows for the elucidation of reactive paths for dissipative, nonadiabatic dynamics when the system is embedded in a Markovian environment. We detail the dominant pathways and rates of thermally activated processes and the relaxation pathways and photoyields following vertical excitation in a minimal model of a conical intersection. We find that the geometry of the conical intersection affects the electronic character of the transition state as defined through a generalization of a committor function for a thermal barrier crossing event. Similarly, the geometry changes the mechanism of relaxation following a vertical excitation. Relaxation in models resulting from small diabatic coupling proceeds through pathways dominated by pure dephasing, while those with large diabatic coupling proceed through pathways limited by dissipation. The perspective introduced here for the nonadiabatic dynamics of open quantum systems generalizes classical notions of reactive paths to fundamentally quantum mechanical processes.

Published under an exclusive license by AIP Publishing. https://doi.org/10.1063/5.0102891

INTRODUCTION

Chemical reactions are largely understood through the identification and enumeration of reactive paths that evolve on potential energy surfaces and over transition states. Such a classical description of reactivity is valid when motion of heavy particles proceeds adiabatically with respect to the electronic degrees of freedom.[1,2] However, if the nuclear and electronic degrees of freedom become correlated and the resultant dynamics are nonadiabatic, classical notions of reactive paths and spatially localized transition states break down.[3–6] Finding an appropriate framework for understanding reaction mechanisms when the dynamics are quantum mechanical remains an outstanding challenge.[7] Here, we provide such a framework in the limit that the quantum dynamics are mediated by a Markovian bath that acts to dephase superpositions and dissipate energy. To accomplish this, we generalize transition path theory[8] developed in the context of classical Markov processes to study a system evolving through its Hilbert space with transitions mediated by a thermal bath. This construction provides a means of defining reactive paths, calculating rates, and determining yields of photochemical processes when the coupling between the system and the bath is weak and the dynamics are nonadiabatic.

Nonadiabatic dynamics occur in photochemical reactions when excitation supplies reactants sufficient energy to access higher lying electronic states.[9] Molecular configurations where multiple adiabatic potential surfaces meet, such as conical intersections or conical seams,[10] necessarily result in a breakdown of the adiabatic or Born–Oppenheimer approximation, yielding a dynamics that convolve nuclear and electronic motion.[11,12] Conical intersections especially play important roles in natural and synthetic systems as they mediate ultrafast nonradiative relaxation.[13–15] In nucleotides, they dissipate dangerous excitations,[16] and in photoswitches, they funnel excitation energy into directed conformational changes.[17] Rates and yields of nonadiabatic reactions are sensitive to changes in the environment.[9,18,19] For example, different solvents can strongly influence the photoyields and mechanisms of azobenzene isomerization as inferred from pump–probe experiments.[20]

When nonadiabatic dynamics occur in condensed phases, the dual importance of nonadiabatic and dissipative effects renders the description of their reactive dynamics necessarily a statistical one.[21–23] This requires a theoretical framework capable of describing the ensemble of reactive paths analogously to that developed within a classical context.

Understanding reaction dynamics in the nonadiabatic limit and in the presence of many interacting degrees of freedom is difficult as many tools for analyzing reaction paths and transition states depend on classical views of the system or the Born–Oppenheimer approximation. Nevertheless, attempts to understand reactive dynamics of open quantum systems have resulted in the development of rigorous, quantum mechanical transition state theories based on time correlation function formalisms.[4,24–26] Such theories can account for low temperature, deep tunneling effects,[6,27–33] and rate expressions can be formulated within an instanton approximation to the real or imaginary time path integral.[6,30,34] These theories, however, are typically focused on a single potential energy surface and not necessarily applicable to studying the complex behaviors around conical intersections. Notable exceptions are so-called nonadiabatic transition state rate expressions, which use Fermi's golden rule with analytical continuation or nonadiabatic extensions to ring polymer instanton theory.[33,35–47] Instanton and lowest order perturbation theories admit the description of only one dominant transition pathway; however, at elevated temperatures or for relaxation following photoexcitation, a broad ensemble of paths is expected to contribute. Some recent work on path-integral based corrections to quantum transition state theory allows for the inclusion of multiple pathways.[46,48–50]

In classical systems, trajectory-based approaches have been successful at distilling reactive dynamics in condensed phase systems through the introduction of transition path ensembles and associated ensembles of transition states.[51,52] Analogous approaches can be adapted to treat quantum systems when the uncertainty is only in the initial condition.[53,54] More generally, uncertainty results from both initial conditions and quantum superpositions, and developing an analogous trajectory ensemble based approach to address both is complicated by the inability to generally define a quantum trajectory under conditions demanding that real, positive probabilities are assigned to each trajectory in order to guarantee equivalent interpretation with a classical ensemble.[55]

A quantum trajectory conveying information of the state of the system at every time is analogous to repeated measurements of the system and, as such, will enforce an evolution which is incoherent.[56] In the limit of weak system–bath coupling, however, quantum jump trajectories can be defined as a time record of wavefunction evolution conditioned on a choice of measurement with different methods of experimental observation corresponding to different stochastic unravelings of a reduced density matrix dynamics.[57] Quantum jumps have been witnessed and manipulated in the lab with their counting statistics observed and even controlled.[57–60] Applications of trajectory-based quantum control, such as randomly resetting the state of propagating trajectories or interfering to rotate away from dark states in Hilbert space, have gained interest, lending credence to quantum jump trajectories as a realizable process which provides insights into quantum phenomena.[57,58,61] However, multiple unravelings of the density matrix exist, and in the absence of the direct invocation of explicit experimental design, the use of any specific stochastic unraveling to aid in the interpretation of the behavior of a quantum system is subjective. Nevertheless, extensions of quantum jumps to chemical dynamics problems have recently been developed[62] allowing the framework of transition path sampling[63] to be brought to bear on questions of proton-coupled electron transfer and thermal barrier crossings and utility derived within that perspective.

Expanding on these previous approaches we generalize the Transition Path Theory (TPT)[8] of classical Markov models to nonadiabatic dynamics employing quantum jump trajectories as the generator of the underlying stochastic process. TPT supplies a number of formal results, allowing for the evaluation of typical reaction paths and locations of dynamical bottlenecks and rate constants.[64,65] It has been used extensively in protein folding to reveal the structure of the folding landscape.[65–68] Here, we use TPT to characterize the behavior of dynamics in the vicinity of a conical intersection. We use quantum jump dynamics to generate a Markov process between energy eigenstates in a linear vibronic coupling model[69] and describe rare reactive dynamics.[70] The experimental equivalent to the jump unraveling employed would involve the measurement of phonons entering and exiting the surrounding bath or the continuous monitoring of the system's energy.[71] From probabilities to react and equilibrium populations of the system, we calculate reactive fluxes between each eigenstate, and from the resulting graph of reactive fluxes we calculate reaction rates, quantum yields, and principally important reaction pathways. We consider thermally activated dynamics and vertical excitations for a variety of conical intersection geometries. We observe an increase of the thermal barrier crossing rate with the increasing diabatic coupling strength and identify a change in mechanism from tunneling at low diabatic coupling to traversing around the conical intersection at high diabatic coupling. The destination of relaxing trajectories following vertical excitation at low diabatic coupling was determined by dephasing effects with the trajectory's fate sealed at high energies, whereas the destination of relaxing trajectories at high diabatic coupling was decided at energies comparable to the barrier, with a larger photoyield and a greater variety of relaxation pathways.

NONADIABATIC REACTIONS IN OPEN QUANTUM SYSTEMS

In order to apply the framework of TPT, we require a dynamics that is dissipative and Markovian. For a quantum system in contact with an infinite heat bath, we focus on the dissipative evolution of a reduced density matrix evaluated by integrating out the bath degrees of freedom. We consider models defined through separable Hamiltonians written as the sum of an operator acting only on the system, H_s, an operator acting only on the bath, H_b, and an interaction term, V, which couples the two.[2] The full Hamiltonian, H, is

$$H = H_s + H_b + V, \tag{1}$$

where the coupling term is taken as bilinear in the system and bath operators,

$$V = Q_t F_t + Q_c F_c, \tag{2}$$

where $Q_{t/c}$ acts within the system's Hilbert space and $F_{t/c}$ acts in the bath's.[72] In the model of a conical intersection we study, we represent two vibrational modes explicitly, the tuning mode Q_t and the coupling mode Q_c. All other vibrational modes are incorporated in the harmonic bath to which the system is coupled through the explicit modes.

Quantum jump dynamics

In the limit that the system and the bath are weakly coupled, the dynamics of the reduced density matrix is Markovian and is well described by a quantum master equation.[73] The specific dynamics we consider are those that result from the Lindblad master equation. The Lindblad master equation derives from second order perturbation theory applied to the system–bath coupling operator followed by the Markovian and secular approximations.[56] The time evolution of a reduced density matrix spanning the system Hilbert's space, $\rho(t)$, is given by a linear operator $\mathcal{D}$,

$$\frac{\partial \rho(t)}{\partial t} = \mathcal{D}[\rho(t)], \tag{3}$$

which is decomposable into two types of terms,

$$\mathcal{D}[\rho(t)] = -\frac{i}{\hbar}[H_s, \rho(t)] + \sum_{a,i,j} \Gamma_{ij}^a \left(L_{ij}^a \rho(t)(L_{ij}^a)^\dagger - \frac{1}{2}\left\{ (L_{ij}^a)^\dagger L_{ij}^a, \rho(t) \right\} \right), \tag{4}$$

where the sum over i, j is over all the eigenstates of the system, a sums over the independent baths to which the system is coupled, and $\hbar$ is Planck's constant. The first term is a coherent portion of the dynamics determined by H_s, which generates a time evolution, provided that the density matrix is not in an energy eigenstate. The second term is an incoherent hopping process that reflects the influence of the bath and leads to irreversible relaxation of the system. The dissipative dynamics are determined by Γ_{ij}^a, the jump rates between states i and j associated with a jump operator L_{ij}^a with Hermitian conjugate $(L_{ij}^a)^\dagger$. Within the energy eigenbasis, the Lindblad equations represent a set of linearly coupled equations for the diagonal elements of the density matrix in the energy eigenstate representation.

Each jump operator, L_{ij}^a, is constructed from a projection matrix onto energy eigenvector subspaces in the energy eigenbasis, $\{|\phi\rangle\}$, and each Lindblad operator is determined from the system–bath coupling such that[62,74]

$$L_{ij}^a = (Q_a)_{ij}|\phi_i\rangle\langle\phi_j| \tag{5}$$

for $i \neq j$, where $(Q_a)_{ij} = \langle\phi_i|Q_a|\phi_j\rangle$. For $i = j$, a single operator

$$L_{ii}^a = \sum_j (Q_a)_{jj}|\phi_j\rangle\langle\phi_j| \tag{6}$$

results in pure dephasing. The Lindblad equation is equivalent to secular Redfield theory[56,74] when the jump rates, Γ_{ij}^a, associated with each operator are obtained from equilibrium bath correlation functions of the form

$$\Gamma_{ij}^a = \int_0^\infty e^{-i\omega_{ij}t} \langle F_a(t)F_a(0) \rangle \, dt, \tag{7}$$

where $\omega_{ij} = (E_i - E_j)/\hbar$ is determined by the energy eigenvalues of the isolated system and $\langle \ldots \rangle$ is the averaging operation. Hopping rates evaluated in this way obey detailed balance and ensure the proper thermalization within the system Hilbert space.[75]

The Lindblad master equation can be viewed as the average evolution associated with a stochastic Schrödinger equation. The unraveled Lindblad equations describe the progression of individual wavefunction trajectories under a Poisson jump process in which wavefunctions transition instantaneously between eigenstates.[76] The stochastic formulation allows for the investigation of reaction pathways and mechanisms of individual trajectories rather than mere inspection of the average behavior of a trajectory ensemble through density matrix evolution.[62] The Lindblad equation may be disassembled into a stochastic equation of motion describing the evolution of a single wavefunction, $\Psi(t)$, as

$$d|\Psi(t)\rangle = -\frac{i}{\hbar}\tilde{H}_s|\Psi(t)\rangle dt + \sum_{a,i,j}\left(\frac{\sqrt{\Gamma_{ij}^a}L_{ij}^a}{\langle\Psi(t)|\Gamma_{ij}^a(L_{ij}^a)^\dagger L_{ij}^a|\Psi(t)\rangle} - 1 \right)|\Psi(t)\rangle dN_{ij}^a, \tag{8}$$

where $dN_{ij}^a = 0, 1$ and $(dN_{ij}^a)^2 = dN_{ij}^a$ characterize the Poisson noise associated with the stochastic process. The effective Hamiltonian of the unraveled formulation

$$\tilde{H}_s = H_s - \frac{i}{2}\sum_{i,j}\Gamma_{ij}^a(L_{ij}^a)^\dagger L_{ij}^a \tag{9}$$

includes an additional, anti-Hermitian summation due to the effects of the jump operators. While the deterministic evolution does not preserve norm, the stochastic evolution restores it on average. The evolution of the reduced density matrix, $\rho(t) = \langle|\Psi(t)\rangle\langle\Psi(t)|\rangle$, can be recovered by averaging over a sufficient number of Lindblad trajectories. The unraveling of the Lindblad equation clarifies that within the eigenstate representation of the system, the evolution of the system is analogous to a classical, continuous time Markov process, and as such, the formal results of TPT can be applied.

Transition path theory

With a stochastic process description of the quantum dynamics afforded by the unraveled Lindblad equation, we will use TPT to resolve the salient features of the resultant reactive dynamics. TPT presents a framework for characterizing the reactive dynamical events of a system described by a Markov process. The central quantity in TPT is the transition matrix, which is the integrated infinitesimal generator.[77,78] The transition matrix has entries $T_{i,j}$ that indicate the probability for state i to transition to state j during time τ.[65] We consider a Markov model spanned by the energy eigenbasis with transition probabilities informed by Lindblad population calculations. Specifically, we calculated $T_{i,j}$ from density matrix propagation beginning from the reduced density matrix $\rho_{ii}(0) = \langle|\phi_i\rangle\langle\phi_i|\rangle$, propagated over a short time τ as

$$T_{i,j} = [e^{\tau\mathcal{D}}\rho_{ii}(0)]_{jj} \approx \{1 + \tau\mathcal{D}[\rho_{ii}(0)]\}_{jj}, \tag{10}$$

where $\mathcal{D}$ is the superoperator defined in Eq. (4). For the systems we consider, τ can be taken arbitrarily small, provided that errors due to

12 February 2024 19:26:52

numerical precision are not encountered, and it should not be taken much larger than the characteristic hopping time between energy adjacent states. The dependence of inferred properties on the choice of τ is explored in Appendix A.

TPT offers a set of relations to evaluate the commitment probability for transitions between an initial set of states, A, referred to here as the reactant state, and a final set of states, B, referred to here as the product state. The commitment probability, or committor, is denoted as $P_{B|A}(i)$, indicating the probability for a system currently in state i to visit the product subset of states B before visiting the reactant subset of states A. Similarly, the probability, $P_{A|B}(i)$, indicates the probability to visit A before visiting B. The reverse committor, $P_{A|B}^*(i)$, is defined as an analogous conditional probability to $P_{A|B}(i)$ but under a time reversed dynamics. In a detailed balance system, the reverse committor $P_{A|B}^*(i)$ is $P_{A|B}^*(i) = P_{A|B}(i) = 1 - P_{B|A}(i)$ due to microscopic reversibility. The committor functions as an ideal reaction coordinate as it conveys exactly the progress of a transition from the reactant state to the product state.[79,80] The collection of states for which $P_{B|A} = 1/2$ is then identifiable as a transition state ensemble as those states have equal likelihood of proceeding to the product state or returning to the reactant state.

When the full matrix of transition rates is computable, the TPT approach is fast and efficient and rigorously assigns the committor probabilities while simplifying the description of the reaction pathways. From the transition matrix, committor probabilities satisfy a backward Kolmogorov equation,[8]

$$P_{B|A}(i) - \sum_{j \in I} T_{i,j} P_{B|A}(j) = \sum_{j \in B} T_{i,j}, \tag{11}$$

with boundary conditions $P_{B|A}(i) = 0$ for $i \in A$ and $P_{B|A}(i) = 1$ for $i \in B$, where I is the set of all states not in A or B.

Once committors have been calculated, the average flux, $f_{i,j}^{A,B}$, between states i and j conditioned on arriving from A and proceeding to B can be found from

$$f_{i,j}^{A,B} = \pi_i P_{A|B}^*(i) T_{i,j} P_{B|A}(j), \quad i \neq j, \tag{12}$$

where by construction $f_{i,i}^{A,B} = 0$ and π_i is the steady-state probability of state i.[65] To find the total reactive flux, F, between A and B,

$$F = \sum_{a \in A, j \notin A} f_{a,j}^{A,B} = \sum_{j \notin B, b \in B} f_{j,b}^{A,B}, \tag{13}$$

the reactive flux leaving A along all possible connections or the reactive flux arriving in B along all possible connections is summed. The thermal reaction rate in the long time limit is found in TPT from F divided by time, τ,

$$k_{A,B} = \frac{F}{\tau \pi_A}, \tag{14}$$

taking into account a factor of π_A, where $\pi_A = \sum_i \pi_i P_{A|B}^*(i)$ is the probability that a system in state i is moving from A to B. In the following, each state in the Markov model will be either an eigenstate of the system or any generic superposition yet to collapse to an eigenstate. In analyzing conical intersection dynamics in the thermal cases, the reactants, A, and products, B, will comprise only a single eigenstate. For relaxation following vertical excitation, we will be interested in the resultant branching dynamics, necessitating further generalization.

The resultant Markov dynamics can be thought of as a graph with the eigenstates as vertices and edge weights given by the reactive flux, $f_{i,j}^+$,[65]

$$f_{i,j}^+ = \max[0, f_{i,j}^{A,B} - f_{j,i}^{A,B}], \tag{15}$$

which encodes the net traffic over time τ between states i and j. An ensemble of reactive pathways through this graph may be selected by first choosing a pathway along edges from A to B and subtracting from each edge in the pathway the flux, f_i, assigned to this pathway, where f_i is equal to the minimum $f_{i,j}^+$ of any i, j transition in the pathway. Another pathway may, then, be assembled from the modified graph in the same manner. Infinitely many ensembles could be assembled in this way. An ensemble of particular interest is the max–min flux ensemble as it repeatedly locates the bottleneck of the graph and incorporates this edge into the next pathway.[8,65] In this scheme, a pathway with the largest possible flux is chosen at each step. A modified Dijkstra's algorithm, employed repeatedly, can locate these pathways.[81]

Since we define reactants and products based on energy eigenstates, the current method requires that the system has low energy eigenstates that are localized in each well. Such definitions would not work for a symmetric system that results in the lowest energy eigenstate or eigenstates being delocalized nor for the case in which the energy barrier is so low that significant mixing of diabatic character occurs in the very lowest eigenstates. In the former case, for large barriers and small couplings, the reactive flux would be insensitive to a small perturbation that would break the symmetry, providing a potential generalization. In the latter case, a steady-state thermal rate would not likely be definable.

LINEAR VIBRONIC COUPLING MODEL

In order to test the utility of TPT for nonadiabatic dynamics, we have studied a linear vibronic coupling model of a conical intersection. The linear vibronic model is a multistate, multimode harmonic oscillator model. Here, we focus on two modes, a tuning mode, Q_t, and a coupling mode, Q_c, which define a conical intersection. The system Hamiltonian is[69] given by

$$H_s = \sum_{k=1,2} |\psi_k\rangle h_k \langle\psi_k| + (|\psi_1\rangle\langle\psi_2| + |\psi_2\rangle\langle\psi_1|)\lambda Q_c, \tag{16}$$

where ψ_k denotes the kth diabatic state. The diabatic states are coupled through Q_c with strength determined by the diabatic coupling λ. Each diabatic Hamiltonian, h_k, is given by

$$h_k = \frac{1}{2}\sum_{j=c,t} \hbar\omega_j\{P_j^2 + Q_j^2\} + E_k + \kappa_k Q_t, \tag{17}$$

where P_j and Q_j are the momentum and position operators of the coordinate j and E_k is a constant energy added to each diabatic potential. The oscillator frequencies are given by ω_j, and tuning oscillator position displacements are given by κ_k. Examples of the resultant adiabatic potential energy surfaces, as well as the energies of lower lying eigenstates, are shown in Fig. 1 for the case of large diabatic coupling. We consider a sufficiently small range of λ such
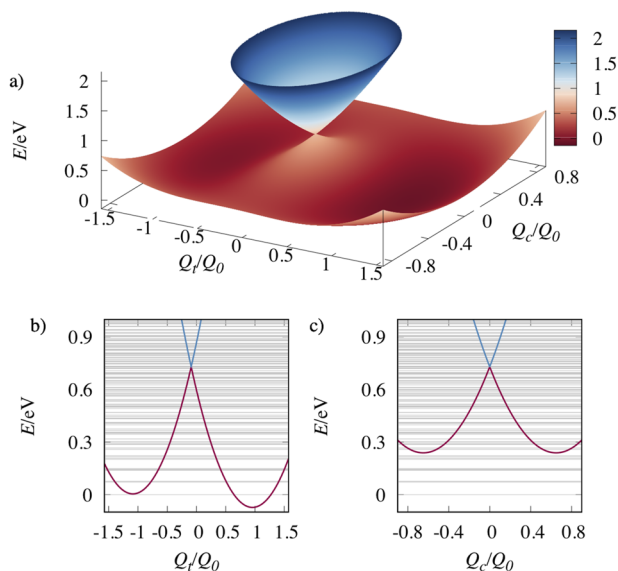
FIG. 1. (a) Adiabatic surfaces for $\lambda = 1.3\lambda_0$ with the color indicating energy. (b) Slice through the conical intersection along $Q_c/Q_0 = 0$ with adiabatic energy surfaces in red and blue and eigenstate energies in gray. (c) Slice through the conical intersection along $Q_t/Q_0 = -0.09$ denoted as in (b).

that there is a barrier in the lower adiabatic potential energy surface that supports localized energy eigenstates within each basin.

The baths coupled to Q_c and Q_t consist of an infinite number of harmonic oscillators,

$$H_B = \sum_\alpha \sum_{j=c,t} \frac{1}{2}\hbar\omega_{\alpha,j}\left(p_{\alpha,j}^2 + q_{\alpha,j}^2\right), \qquad (18)$$

where $p_{\alpha,j}$ and $q_{\alpha,j}$ refer to the momentum and coordinate of the αth harmonic oscillator in the bath coupled to the jth mode in the system. The system–bath coupling is bilinear such that

$$V = \left(|\psi_1\rangle\langle\psi_1| + |\psi_2\rangle\langle\psi_2|\right)\sum_\alpha \sum_{j=c,t} c_{\alpha,j}q_{\alpha,j}Q_j, \qquad (19)$$

where $c_{\alpha,j}$ is the coupling strength of each oscillator. The coupling of the system to the bath is summarized by a spectral density of the Debye form,

$$
\begin{aligned}
J_j(\omega) &= \sum_\alpha c_{\alpha,j}^2 \delta(\omega - \omega_{\alpha,j}) \\
&= 2\eta \frac{\omega\omega_b}{\omega^2 + \omega_b^2}, \qquad (20)
\end{aligned}
$$

where ω_b is the cutoff frequency and η is the reorganization energy, which is taken to be small.

The specific parameters we have employed for this model are reminiscent of a parameterization for the photoisomerization of pyrazine.[82] However, in order to produce a metastable, double-well structure in the ground adiabatic state, we increased the displacement of both oscillators relative to the parameters previously used and adjusted the relative energies of the diabatic electronic states. See Table I for specific parameters employed. Of particular importance

TABLE I. Simulation parameters for the linear vibronic coupling model.

Parameter	Value (eV)
Tuning mode frequency ω_t	0.074
Coupling mode frequency ω_c	0.118
State 1 displacement κ_1	0.358
State 2 displacement κ_2	−0.315
State 1 energy shift E_1	4.21
State 2 energy shift E_2	3.94
Reference diabatic coupling λ_0	0.262
Characteristic bath frequency ω_b	0.013 16
Reorganization energy η	2.628×10^{-4}

will be the impact of the diabatic coupling strength λ on the reactive dynamics in the vicinity of the conical intersection. The magnitude of λ has a dramatic impact on the conical intersection geometry, particularly on the adiabatic potential energy barrier height. The value of λ is frequently changed by a multiple throughout this work with λ_0 being the value found in the unaltered pyrazine model, $\lambda_0 = 0.262$ eV. To simplify figures, we define Q_0 as the average of $|Q_t|$ of the lowest eigenstates, respectively, localized in each diabatic state in the $\lambda = 1.3\lambda_0$ system.

THERMAL BARRIER CROSSINGS

We first consider the transition paths and reactive rates associated with a thermal barrier crossing in the vicinity of a conical intersection. Employing TPT within a Markov model spanned by the energy eigenstates, we abstract away complications associated with defining reactive paths in the presence of both nuclear quantum effects and nonadiabatic effects. Rather than consider reactive paths localized in position space, the paths are defined through a sequence of states localized in energy. In the limit of a high barrier, we expect to recover results from quantum instanton theory.[33,35]

For a thermal transition, the system evolves with a detailed balance dynamics with an incoherent initial condition. In this case, TPT can be used straightforwardly. For concreteness, we consider transitions between the lowest energy eigenstates localized in each diabatic state and designate them as L and R, with R being the lowest energy eigenstate in the system. The specific states depend on λ. Microscopic reversibility guarantees that reactive pathways from L to R are direct inverses of reactive pathways from R to L, making the direction of barrier crossing under study irrelevant.

Typical behavior

Figure 2(a) shows the population in R where $\rho_R(t) = \langle|\phi_R\rangle\langle\phi_R|\rangle$, following initialization of the system in L under density matrix evolution. Two different λ values are displayed, and although ρ_R increases more quickly with time for the larger $\lambda = 1.3\lambda_0$ case, over 1 ps a negligible population has accumulated in R. For the lower coupling, $\lambda = 0.3\lambda_0$, the accumulation of population is many orders of magnitude smaller. This slow rise in population reflects the large adiabatic barrier separating R and L with a concurrent small rate constant. The barrier height sensitively depends on the size of λ, decreasing rapidly as λ increases. Apart
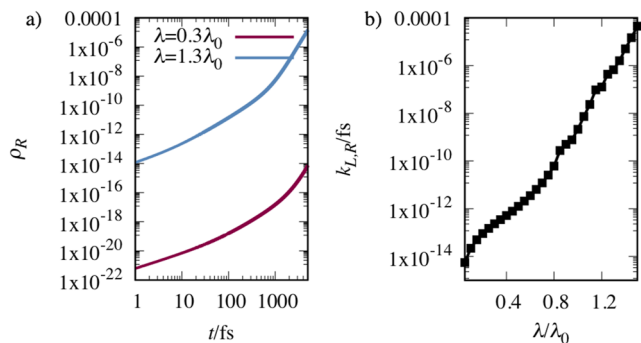
FIG. 2. (a) Population in state R, ρ_R, as a function of time from density matrix dynamics initialized in L for low and high λ systems. (b) Rates of population transfer between L and R, $k_{L,R}$, as a function of λ.

from this slow increase in population, there are no other discernible features in the average dynamics.

The rate constant $k_{L,R}$ for the barrier crossing event from L to R calculated using Eq. (14) is shown in Fig. 2(b). The rate constant increases monotonically with the increasing coupling strength. For very small coupling, the rate constant grows in proportion to λ^2 as expected from perturbation theory, but the domain of that scaling relationship is small $\lambda/\lambda_0 \ll 1$. For larger λ, the rate increases rapidly with a mechanism that from the mean wave packet propagation is not easily discernible.

Transition path ensemble

Each pathway in the TPT max–min flux decomposition of pathways from R to L carries flux f_i. These paths represent the transition path ensemble. The diversity of paths, and their corresponding weights, can be understood by rank ordering the paths based on their flux. The cumulative flux fraction accounted for by the first n highest flux pathways in the decomposition

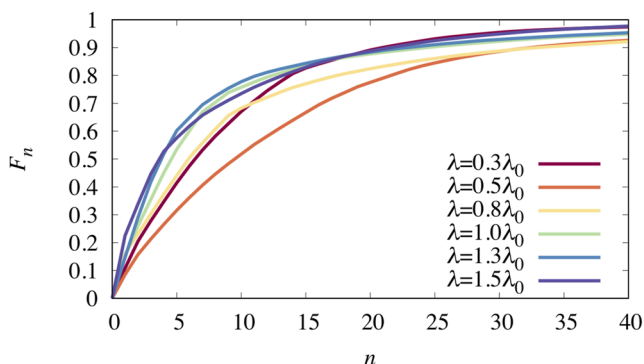$$F_n = \frac{1}{F} \sum_{i=1}^{n} f_i \qquad (21)$$

FIG. 3. The number of thermally calculated pathways, n, required to account for a given fraction, F_n, of the overall thermal flux between R and L for several values of λ.

is a direct measure of the number of relevant pathways in the transition path ensemble.[65] Figure 3 shows F_n for several different λ values. In this system, likely as a result of the large barrier in the lower adiabatic potential, the majority of the reactive flux, regardless of diabatic coupling strength, is accounted for by the first few pathways. This manifests the approach of the instantonic limit as the barrier height is large compared to both thermal energy and the zero point energy in the tuning mode. As the barrier becomes large, only few paths contribute significant weight to the reactive path ensemble. Because in this thermally activated process there are clearly a few dominant pathways, these can be inspected more closely to discover the most prevalent transition mechanisms at different coupling strengths.

Dominant transition paths

We inspected some of the prominent transition pathways for mechanistic information. We considered the transition path from L to R with maximum f_i at several λ values. Figure 4 shows the committor, $P_{L|R}(i)$, for each step in the pathways, meaning the probability at each step for the system to return to eigenstate L. The principle paths are the most likely sequences of states along a reactive quantum jump trajectory but do not retain direct temporal information. To recover a typical timeseries, these paths would need to be convoluted with the appropriate waiting time distributions at each step. Nevertheless, the sequence of states retains significant mechanistic information.

At low λ, the transition pathways involved more quantum jumps with the dominant pathway at $\lambda/\lambda_0 = 0.3$ requiring 16 jumps compared to 9 for $\lambda/\lambda_0 = 1.3$. As λ increased, the transition eigenstates, the states just prior to and just after commitment defined at $P_{L|R} = 1/2$, became closer to $P_{L|R} = 1/2$, more mixed in terms of diabatic character and less localized in either well. This behavior can be understood as the states near the conical intersection are nearly degenerate and more susceptible to delocalization with increasing λ. In all cases, a single quantum jump, interpretable as a barrier crossing event, resulted in a large change in the average committor value. The abrupt transitions reflect tunneling contributions to the reaction paths as quantum mechanically the system need not actually pass through intermediate states to move from one side of the barrier to another.
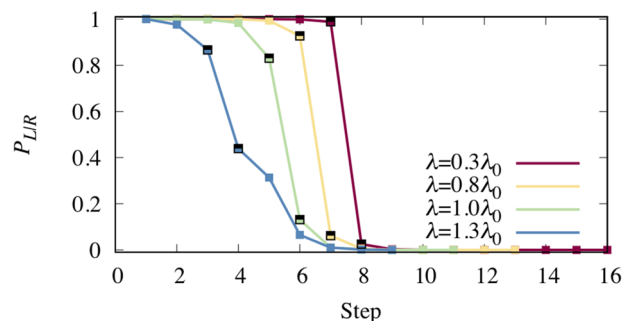

FIG. 4. Dominant thermal barrier crossing pathways showing the probability to commit to L, $P_{L|R}$, for several λ. Filled symbols denote the transition wavefunctions just prior to and after committing.

We inspected the wavefunctions along the barrier crossing pathways and found that low and high λ resulted in significantly different behaviors. Figures 5 and 6 show the energy, E, as a function of step along the dominant reaction pathways for different λ values and the transition eigenstate wavefunctions projected onto each of the diabatic electronic states. In the low λ limit in Fig. 5, both transition eigenstate wavefunctions are similar to harmonic oscillator wavefunctions. They show negligible overlap in density, and their energies are well below the barrier height, which is ~0.7 eV, although the energies of the transition eigenstates are still quite high. This indicates a deep tunneling barrier crossing mechanism and is consistent with sharp changes in position and diabatic character at the transition.

In the high λ limit in Fig. 6, the transition pathway was relatively short, passed through eigenstates with energies nearly equal to the height of the barrier at ~0.24 eV, and involved transition eigenstate wavefunctions, which did not resemble harmonic oscillator wavefunctions but rather showed significant mixing of both diabatic states. Transition wavefunctions are far less localized in either well with the significant density at the barrier of the conical intersection. This indicates that barrier crossing takes place by going around the conical intersection rather than by tunneling through it. These pathways are representative of the behavior of the ensemble although some prominent tunneling pathways remain.

The dominant paths found here are conceptually similar to the dominant pathways produced by the path integral instanton method.[33,83] Previous work of Ranya and Ananth and also Cao and Voth using nonadiabatic instanton theory to analyze the reactive behavior in an avoided crossing and spin-boson model noted that, at smaller diabatic coupling, sharper transitions between diabatic states are observed.[33,83] Cao and Voth also observed an increase in the electron transfer rate with increasing diabatic coupling strength
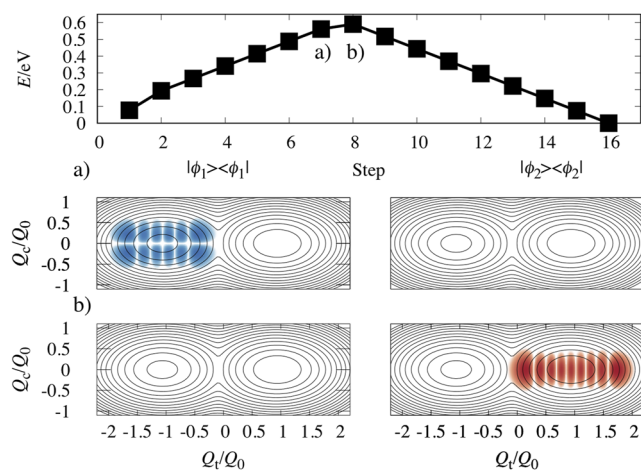

FIG. 5. (top) The energy at each eigenstate along the highest f_i thermal transition pathway between L and R with $\lambda = 0.3\lambda_0$. (bottom) Transition wavefunction densities for the state before $P_{R|L}$ exceeds 1/2 (a) and after $P_{R|L}$ exceeds 1/2 (b) plotted on a logscale. Red indicates the density in diabatic state 2, and blue indicates the density in diabatic state 1. Superimposed on the transition wavefunctions are the lower adiabatic potentials with contours placed at intervals of 0.136 eV.
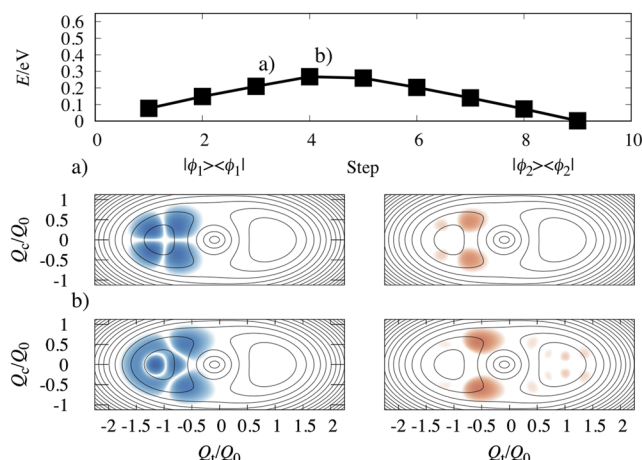

FIG. 6. (top) The energy at each eigenstate along the highest f_i thermal transition pathway between L and R with $\lambda = 1.3\lambda_0$. (bottom) Transition wavefunction densities for the state before $P_{R|L}$ exceeds 1/2 (a) and after $P_{R|L}$ exceeds 1/2 (b) plotted on a logscale. Red indicates the density in diabatic state 2, and blue indicates the density in diabatic state 1. Superimposed on the transition wavefunctions are the lower adiabatic potentials with contours placed at intervals of 0.136 eV.

and noted two regimes, a golden rule regime and an adiabatic limit regime, the latter of which results in a much stronger dependence of rate upon diabatic coupling strength. These trends are consistent with our observations.[83]

The trend observed in the representative pathways suggests that tunneling is the main barrier crossing mechanism at low λ, and traversing around the conical intersection is the main barrier crossing mechanism at high λ. This interpretation is evident in Fig. 7, which displays the energy of the transition eigenstates vs λ relative to the height of the bare lower adiabatic potential barrier. Note that all thermal data were generated from exact density matrix propagation, so there are no statistical errors. The sharp features in Fig. 7 arise from accidental degeneracies between low-lying energy eigenvalues.

At low coupling, the average energy has little dependence on λ and is found far below the barrier. These eigenstates below the barrier display little mixing between electronic states and are highly localized in one well or the other. Deep tunneling is the only feasible reaction pathway when the barrier is so high. This is a very slow mechanism, as demonstrated in Fig. 2, where low coupling results in slow population transfer between L and R and a low $k_{L,R}$. As λ increases, the average energy of transition eigenstates for the ensemble approaches that of the barrier, leading to more delocalization and shallower tunneling mechanisms. The transition eigenstate energies surpass the barrier at the highest coupling strengths only. The barrier crossing proceeds in this case by going around the conical intersection, a significantly faster mechanism that results in more mixing of electronic character in the transition eigenstates.

The transition between the small and large λ limits corresponds to an end of the golden rule regime where the rate scales like λ^2. Such a regime approximately requires that λ is small relative to the frequency of the coupling coordinate though a full accounting on the non-Condon effects at finite temperature complicates a simple analytical picture.[35,84] By constructing transition matrix elements
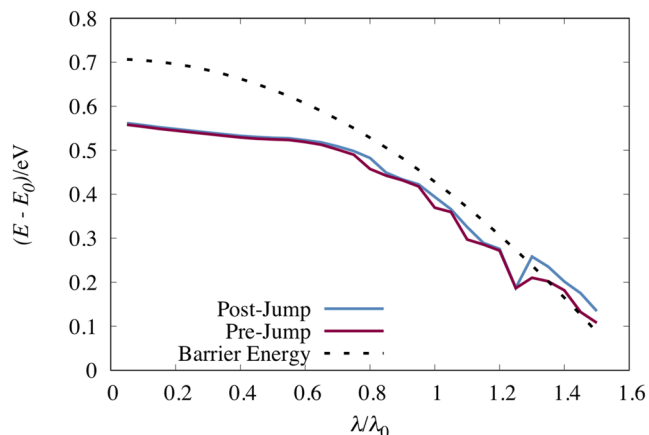
FIG. 7. Average energy relative to E_0, the energy of the lowest eigenstate for the given system, of the transition eigenstates, post-jump and pre-jump, and barrier height during the thermal barrier crossing as a function of λ/λ_0 averaged over the transition path ensemble.

directly from the eigenstate wavefunctions, we maintain any relevant phase relationships upon transitions around the conical intersection such as those due to the generation of a geometric phase.[85] Employing the procedure in Ref. 86, we find that geometric phase effects in the large λ case are small, suppressing the rate by only around 1% for the $\lambda = 1.3\lambda_0$ case.

RELAXATION FOLLOWING VERTICAL EXCITATIONS

Although the equilibrium behavior of a conical intersection system is relevant to thermal isomerizations of photoswitches, it is typically the relaxation following vertical excitation that is of more interest as the energy for spontaneous isomerization is large and much more readily accessed through photoexcitation than thermal fluctuation. Upon photoexcitation, a barrier crossing is no longer rare though during relaxation unlikely events may cause trajectories to favor one potential product state over another. The commitment of a relaxing trajectory to one well or another of the conical intersection can, thus, be a non-equilibrium rare event. While the bulk of the machinery of TPT is not applicable, some ideas for trajectory analysis can be applied to distill the complicated system dynamics. The committors are independent of the initialization of the system, but density matrix propagation information alone is no longer sufficient to analyze relaxation from a vertical excitation because the initial distribution is not stationary. Because the dynamics are Markovian, the transition matrix still provides complete information about the subsequent relaxation, but the uncollapsed wavefunction following vertical excitation requires special consideration.

To study relaxation from a vertical excitation, we consider an initial condition generated from a projection of the lowest energy vibrational eigenstate of a harmonic oscillator located at $Q_i/Q_0 = 0$ for $i = c, t$ with the same frequencies as employed in Eq. (17) into diabatic state $|\phi_1\rangle$. Such a condition has been studied previously in the context of the pyrazine model we have adapted[82] and is meant to approximate the excitation from the ground state into a manifold of excited states. Through the application of suitably

generalized TPT methods to the vertical relaxation case, we are able to determine how relaxing trajectories subsequently commit to one well or another, employing our previous definitions of the R and L states.

Typical behavior

We observe the typical behavior of the system in Fig. 8(b) which displays the average relaxation from direct density matrix propagation following vertical excitation for two λ values. The population in diabatic electronic state 2, $\rho_2 = \langle|\psi_2\rangle\langle\psi_2|\rangle$, shows comparatively quick relaxation toward its equilibrium population with the fast oscillations indicative of Q_t vibrations. Significantly larger but more quickly damped oscillations are seen for the relaxation at higher coupling strength, $\lambda = 1.3\lambda_0$. The higher coupling strength also results in a larger proportion of population relaxing into diabatic well 2. Both the increase in speed of relaxation and the increase in proportion of trajectories which change diabatic state during relaxation with increasing λ are expected from perturbation theory.

We also study the average photoyield, computed using a first passage procedure, whereby states R and L are fixed as absorbing boundary conditions. In practice, this was computed using 10 000 Lindblad jump trajectories initialized in the vertically excited state shown for $\lambda = 1.3\lambda_0$ in Fig. 8(a). The slight asymmetry in the initial wavepacket is a consequence of basis truncation. The photoyield, $\rho_R(t = t_f)$, where t_f is the time at which a trajectory first reaches either R or L, is the fraction of trajectories that end in R without visiting L. Figure 8(c) displays the photoyield as a function of λ. Generally, we find that the photoyield increases with increasing λ although the trend is noisy. Standard deviations estimated from
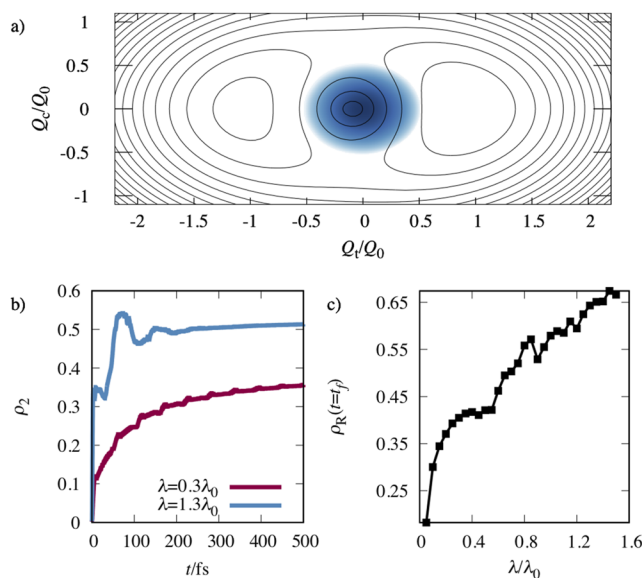

FIG. 8. (a) Initial, vertically excited wavepacket density on a log scale with all density being found in diabatic state 1 depicted in blue. (b) Average diabatic state 2 population, ρ_2, for two extreme coupling strengths following vertical excitation into diabatic state 1. (c) Photoyield of state R, $\rho_R(t = t_f)$, following vertical excitation into diabatic state 1 at various λ.

block averaging are on the order of 0.005. Non-monotonic behavior arises from accidental degeneracies and the change of mechanistic regimes. The plateaus of ρ_2 in Fig. 8(b) and the ρ_R values for the same λ in Fig. 8(c) are not exactly the same. Not only do these values represent different projections of the wavefunction, but ρ_2 as a function of time from density matrix calculations can include recrossing events between eigenstates R and L and the contribution of uncollapsed wavefunctions. As in the thermal case, little detail of the underlying dynamics is forthcoming from the density matrix propagation alone.

Generalization of TPT

In order to apply TPT to a vertically excited initial condition and to study the subsequent branching of the relaxing trajectories, we generalize the TPT framework previously presented. To study the branching of a relaxing stochastic process into distinct basins we define committor functions slightly more generally. Rather than define forward and backward committors as complements of each other, we consider trajectory ensembles in which the system relaxes from some initial state C into a specific product state L or R without visiting the opposing product state. This implies that the forward committor for product state R is defined as the probability of reaching R from state j before returning to C or reaching L, denoted as $P_{R|CL}(j)$. The corresponding backward committor is defined as the probability in the time reversed dynamics of reaching the initial state C before states R or L, denoted for state i as $P^*_{C|RL}(i)$. Under such conditioning, the reactive flux into state R is given by

$$f_{i,j}^{C,R} = P^*_{C|RL}(i)\pi_i T_{i,j} P_{R|CL}(j), \tag{22}$$

where an equivalent formulation can be made for trajectories bound for L.

In addition, the initial condition upon vertical excitation is, in general, a coherent superposition that is irreversibly decohered by the action of the bath. Prior to decoherence, there is not a simple classical means of describing the state of the system from which to evaluate a transition probability using Eq. (10). The state of the system is uncertain with delicate phase relationships between the energy eigenstates. Determining the likelihood of any member of the superposition would require a projective measurement and, thus, loss of the superposition. However, immediately after the state has spontaneously decohered, the system can be described by a classical probability distribution on the energy eigenstates albeit one that is not Boltzmann distributed and, thus, not stationary under the Lindblad operator.

In order to apply TPT, we thus restrict our attention to the Markovian jump dynamics following decoherence and employ an empirical initial distribution generated by evaluating the collapse probabilities into each eigenstate from the initial coherent state conditioned on the final destination of the trajectory. Since the wavefunction collapse is statistical, with significant collapse probabilities into several different eigenstates, it is necessary to scale the reactive flux $f_{i,j}^{C,R}$ by its contribution to the total reactive path ensemble. The contribution of the flux from a specific initial collapsed state C is proportional to the probability for the wavefunction to collapse into eigenstate C, denoted as $\Pi(C)$, and normalized by the total reactive

flux $F^{C,R} = \sum_{j \neq C,L} f_{C,j}^{C,R}$ for eigenstate C. With this weight, the reactive flux is given by

$$f_{i,j}^R = \sum_C f_{i,j}^{C,R} \frac{\Pi(C)}{F^{C,R}} \tag{23}$$

in the conditioned ensemble bound for R. The probability for the wavefunction to collapse into C could be calculated from a conditioned ensemble of Lindblad trajectories. Then, TPT could be performed for each eigenstate C as detailed above to determine $f_{i,j}^{C,R}$. Due to the exponential factors in π_i, solving for $f_{i,j}^{C,R}$ is very numerically unstable. Instead of evaluating them and then constructing the conditioned fluxes directly, we sampled trajectories in conditioned ensembles and estimated $f_{i,j}^R$ by counting how many jumps are made between each pair of eigenstates i and j. The same trajectory ensemble used to compute the photoyields was used for this purpose.

Transition path ensemble

We trace dominant pathways to R through a graph assembled from the ensemble of trajectories ending in R with the edge weights given by $f_{i,j}^{R+} = \max[0, f_{i,j}^R - f_{j,i}^R]$ and then perform the same procedure for trajectories ending in L. Note that the rare case in which the first eigenstate on the pathway is also the destination eigenstate is handled in exactly the same way as all other cases and results in a path consisting of a single jump. Generally, the ensemble of reactive trajectories is much broader than that observed in the thermal reaction. Figure 9 shows the cumulative flux accounted for by the first n highest flux pathways in the conditioned ensemble. As the diabatic coupling strength increases, F_n as a function of n flattens out, meaning that more pathways are required to account for a given total flux. Ten trajectories are sufficient to account for half of the total flux for the weakest coupling, compared to 100 for the strongest coupling. This indicates that at lower coupling strength, the variety of pathways available for relaxation is more limited.

The larger number of pathways at higher coupling is manifested in the much higher number of jumps typically observed during relaxation. The number of inter-eigenstate jumps per trajectory is broader with a higher average for higher λ, with a typical number of jumps of 70 for $\lambda = 1.3\lambda_0$ compared to 10 for $\lambda = 0.3\lambda_0$. As the
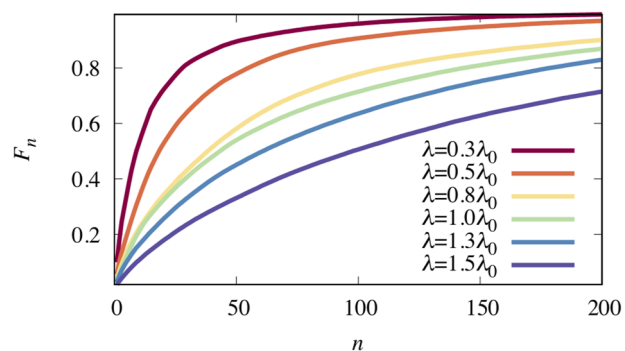

FIG. 9. The number of vertical relaxation pathways, n, required to account for a given fraction, F_n, of the overall flux into L for several values of λ.

coupling to the bath is the same, the larger number of jumps reflects the denser energy eigenstate structure for large λ, where far more favorably sized energy gaps are accessible.

Characteristic transition pathways

While the distribution of reactive trajectories upon vertical excitation is broad, we can, nevertheless, glean information about the mechanism of branching by considering typical transition paths. Figure 10(a) shows $P_{R|L}$ along dominant relaxation pathways to eigenstate R following vertical excitation for several λ values. Figure 10(b) shows the compliment $P_{L|R}$ along dominant relaxation pathways to eigenstate L. Immediately upon dephasing to an eigenstate, low λ trajectories have committors above 1/2. Low λ trajectories bound for L have $P_{L|R}$ approaching 1.0, indicating that dephasing prior to collapse plays a critical role in determining the outcome of these trajectories even though the state to which they initially collapse is still very high in energy. In the case of higher λ, collapse to a moderate $P_{L|R}$ or $P_{R|L}$ eigenstate is followed by jumps that do not alter the committor value and then an abrupt ascent toward a committor value of 1.0. For the strongest coupling case, this is instantonic, superficially similar to the equilibrium case. For high λ, dephasing seems to be far less important and a set of critical jumps much later decides a trajectory's outcome. More insight into the nature of these jumps can be extracted from a closer inspection of the energies and wavefunctions along the relaxation pathways.
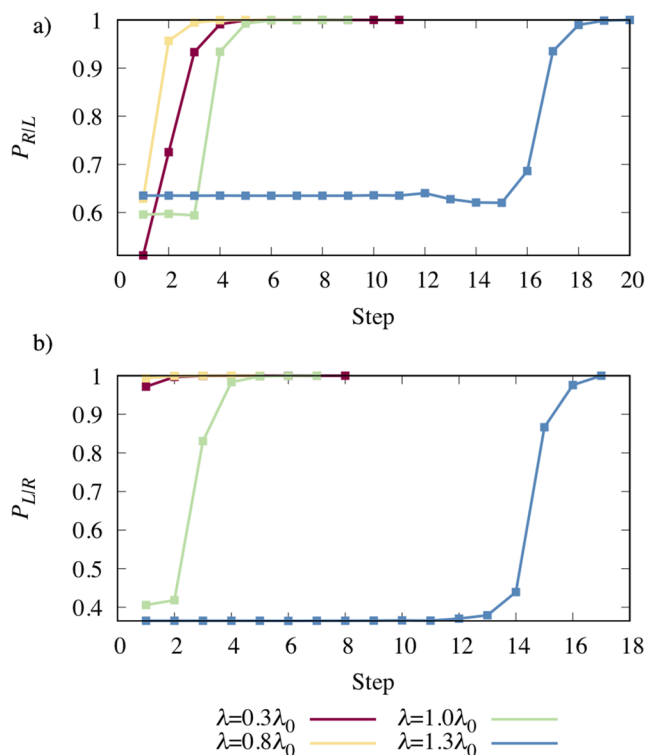

FIG. 10. Dominant vertical relaxation pathways ending in R and L along with their respective committors, $P_{R|L}$ (a) and $P_{L|R}$ (b).

Figures 11 and 12 show the relaxation pathways to L and R following vertical excitation for weak and strong coupling strengths. In each, we show the energy of the eigenstates along the most likely pathway and the wavefunctions projected onto each of the diabatic electronic states for wavefunctions at collapse and after some relaxation, save in the sole case where committor eigenstates can be defined, in which case these states are shown.

Consider the example trajectories from $\lambda = 0.3\lambda_0$. The decision to commit to R or L is made during dephasing with the trajectory committed when it collapses into a single well. This is evident in Fig. 11 from the harmonic oscillator-like wavefunction centered in well 1 for the trajectory ending in state L. The trajectory bound for R is likewise committed and mostly localized to a single well upon collapse although it does have a small amount of diabatic state 1 character, which quickly disappears as relaxation progresses.

At large coupling, $\lambda = 1.3\lambda_0$, collapses to eigenstates of high energy relative to the barrier are common. As most high energy eigenstates are committed to R in this system, most trajectories, including the examples of trajectories relaxing into L and R, collapse into eigenstates for which $P_{R|L}(i)$ exceeds 1/2. The states into which these pathways collapse are highly delocalized, as evident in Fig. 12. It is only after much energy loss through many quantum jumps that the wavefunctions settle into one well or another. At large λ, commitment to L occurs only after the eigenstate energy becomes comparable to the barrier height. The transition eigenstates in the left panels of Fig. 12 have comparable energy to the barrier and have significant density in both diabatic states, but the state for which $P_{L|R}$ surpasses 1/2 has less density in the vicinity of the barrier and is more localized in the metastable well to which it has committed.

Because the wavefunction pre-committor jump may be uncollapsed, statistics about the energy of the state just before the committor surpasses 1/2 could not be reliably collected. However, the post-committor jump eigenstate was available for inspection and its energy for trajectories bound for state L compared with the barrier height at various λ is displayed in Fig. 13. The largest standard deviations estimated from block averaging are on the order of one percent of the average. Accidental degeneracies and the complex interplay of different relaxation pathways lead to the non-monotonic behavior. As in the thermal case, there are two characteristic regimes, with a smooth crossover between them. At low coupling, the post-committor eigenstate has energy significantly above the barrier on average. At higher coupling, the post-committor eigenstate has energy comparable to the barrier, supporting the trend shown in the example trajectories where low λ systems commit during dephasing and at high energies, whereas high λ systems commit following dephasing and dissipation until the wavefunction's energy is comparable to that of the barrier. Comparing Fig. 13 with the photoyields in Fig. 8(b), a lower photoyield is associated with commitment by dephasing, with an apparent regime change at approximately $\lambda/\lambda_0 = 0.6$. Dephasing commitment provides fewer opportunities to change diabatic states compared to dissipative commitment, a trend reinforced by the larger variety of relaxation pathways observed for higher λ in Fig. 10.

Lindblad dynamics naturally separates out the effects of the dephasing operator from dissipative operators. Pure dephasing effects have been studied extensively[87–92] with studies exploring
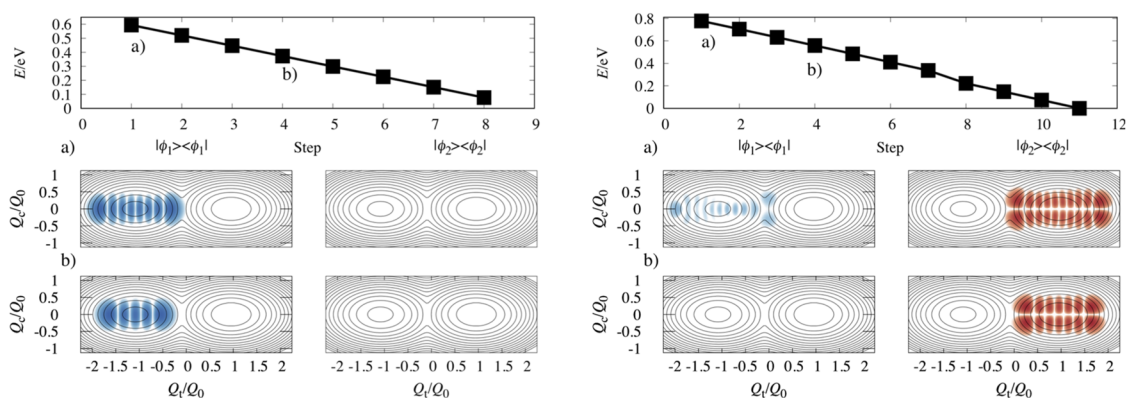
FIG. 11. (top) The energy at each eigenstate along the dominant relaxation pathway into L (left) and R (right) when $\lambda = 0.3\lambda_0$. (bottom) The wavefunction density just after collapse into an eigenstate (a) and the wavefunction density following some relaxation (b) plotted on a log scale. All wavefunctions are committed. Blue indicates the density in diabatic state 1, and red indicates the density in diabatic state 2. Superimposed on the wavefunctions are the lower adiabatic potentials with contours placed at intervals of 0.136 eV.
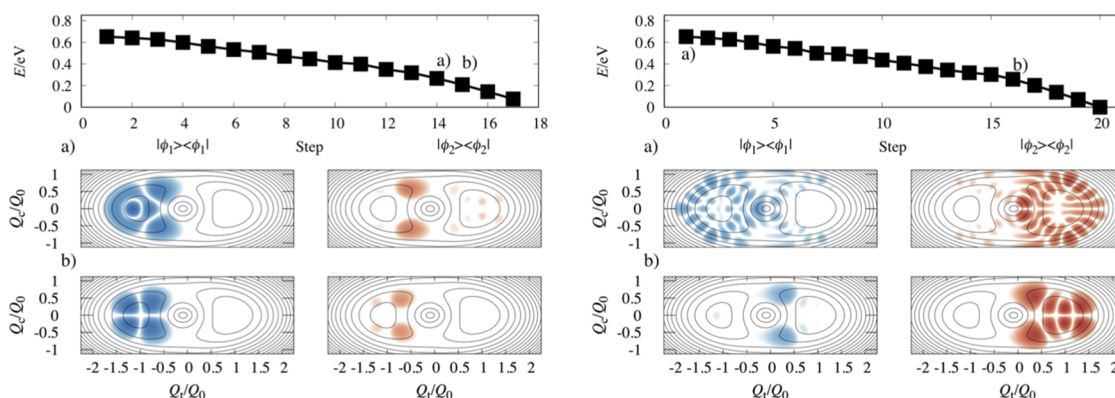

FIG. 12. (top) The energy at each eigenstate along the dominant relaxation pathway into L (left) and R (right) when $\lambda = 1.3\lambda_0$. (bottom) Transition wavefunction densities for the state before $P_{L|R}$ exceeds $1/2$ (a) (left) and after $P_{L|R}$ exceeds $1/2$ (b) (left) plotted on a log scale. The wavefunction just after collapse into an eigenstate (a) (right) and the wavefunction density following some relaxation (b) (right). Blue indicates the density in diabatic state 1, and red indicates the density in diabatic state 2. Superimposed on the wavefunctions are the lower adiabatic potentials with contours placed at intervals of 0.136 eV.

dephasing and decoherence effects in many different systems.[93–98] The importance of dephasing and decoherence to dynamics in more complicated systems such as excitons and conical intersections has been demonstrated.[99,100] By inspecting the dominant relaxation pathways following vertical excitation, we observe the effects from dephasing separately from dissipation and determine that the action of the dephasing operator decides the fates of trajectories when λ is small. The importance of dephasing effects is not surprising as Heller *et al.* recently studied fewest switches surface hopping trajectories through a conical intersection with various decoherence corrections and determined that the method of correction employed could have a dramatic and not easily predictable impact on the population dynamics of individual trajectories.[100]

Previous work investigating the effect of modifying λ on behavior at conical intersections has uncovered similar trends as observed here.[101,102] Lan and co-workers, employing multi-level Redfield theory with most of the molecules' internal modes comprising the bath, found λ to be a limiting parameter on the rate of internal conversion following vertical excitation of the pyrrole–pyridine complex. Doubling λ, doubled the rate of internal conversion.[101] This limiting behavior of λ is consistent with our results, which show λ's striking influence on the quantum yield. Manthe and Koppel investigated the closed system wavepacket dynamics of several different molecules with accessible conical intersections, including $C_6H_6^+$ and NO_2 following vertical excitation. Classes of behavior based on λ were assigned with the small λ regime showing largely diabatic behavior, the large λ regime showing largely adiabatic behavior, and an intermediate regime sometimes resulting in complicated interplays of adiabatic and diabatic effects.[102] These results are more difficult to compare to this work; however, a striking
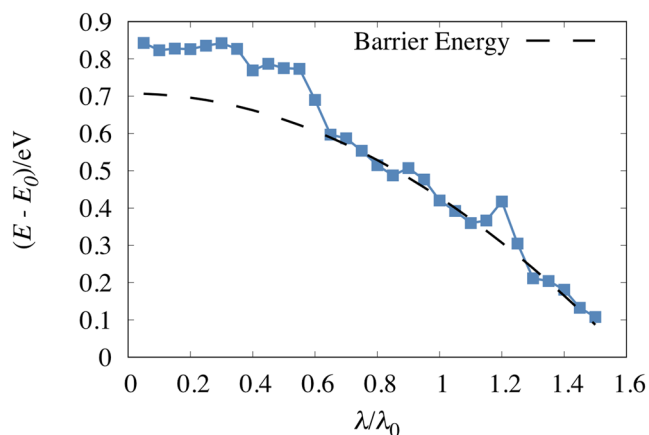
FIG. 13. Energy relative to the lowest energy eigenstate immediately following the jump at which the trajectory in the ensemble conditioned to end in L first visits an eigenstate for which $P_{L|R} \geq 1/2$ and the barrier height for comparison.

change in the regime between small and large λ is visible in this investigation and that of Manthe and Koppel.[102]

CONCLUSIONS

By generalizing TPT to Lindblad dynamics as a means of characterizing committor probabilities of eigenstates and typical quantum transition pathway hopping through energy space, we have elucidated the effect of diabatic coupling strength on dynamics at conical intersections. In a thermal barrier crossing, a larger λ results in a higher rate of population transfer between the metastable and stable well. The committors for each eigenstate of the system and principle paths to analyze for mechanistic information provided by TPT reveal that the energy of the conical intersection itself is never reached during barrier crossing events. Rather, we find that when λ is small deep tunneling is principally responsible for population transfer between the stable and metastable well, whereas when λ is large traversing around the conical intersection is principally responsible.

By applying a modified TPT approach to treat relaxation following a vertical excitation, we find that increasing λ greatly increases the diversity of the relaxation pathways available to the system and results in many quantum jumps whose purpose is merely to dissipate energy prior to commitment to one well or another. Analysis of pathways of principal importance at several λ values reveals that the fate of low λ trajectories is largely determined during dephasing, meaning that a trajectory bound for eigenstate L typically has committed upon the collapse of the wavefunction to an eigenstate, whereas at higher λ trajectories typically relax and lose energy until comparable with the adiabatic potential energy barrier before committing.

These fundamental differences in behavior between low and high λ systems imply a trade-off. High λ systems have a high photoyield, but experience a fast thermal barrier crossing by going around the conical intersection. Low λ systems have low photoyields, but must cross the barrier by slow, deep tunneling mechanisms.

Although limited by the weak coupling assumption, we have, nevertheless, provided a means of studying reactions in highly nonadiabatic regimes. This work opens avenues of exploration into the dynamics of conical intersections and other systems. This generalization of transition path theory to quantum dynamics shows promise for elucidating mechanisms in a variety of circumstances and contributes a useful view of quantum transition pathways.

AUTHOR DECLARATIONS

Conflict of Interest

The authors have no conflicts to disclose.

Author Contributions

Michelle C. Anderson: Conceptualization (equal); Data curation (equal); Formal analysis (equal); Investigation (equal); Methodology (equal); Writing – original draft (equal); Writing – review & editing (equal). **Addison J. Schile**: Investigation (equal); Methodology (equal); Writing – review & editing (equal). **David T. Limmer**: Conceptualization (equal); Formal analysis (equal); Funding acquisition (equal); Investigation (equal); Methodology (equal); Project administration (equal); Writing – original draft (equal); Writing – review & editing (equal).

DATA AVAILABILITY

The data that support the findings of this study are openly available in Zenodo at http://doi.org/10.5281/zenodo.6950371v2.[103]

APPENDIX A: MODEL DETAILS

The modified conical intersection based on a pyrazine parameterization[82] is specified in Table I. The Q_c basis includes 40 unshifted harmonic oscillator basis functions, and the Q_t basis includes 110 unshifted harmonic oscillator basis functions, save in the case of density matrix propagation initialized in an eigenstate, which employs 30 and 80, respectively. Thermal equilibrium calculations include a truncated basis of 700 energy eigenstates, save in the case of density matrix propagation initialized in an eigenstate, which uses a truncated basis of 240 energy eigenstates. Vertical excitation calculations employ a truncated basis of 700 energy eigenstates, save in the case of vertical density matrix propagation, which employs a truncated basis of 800 energy eigenstates. A total of 10 000 vertical relaxation trajectories are simulated at each coupling strength. The temperature for all simulations is 300 K.
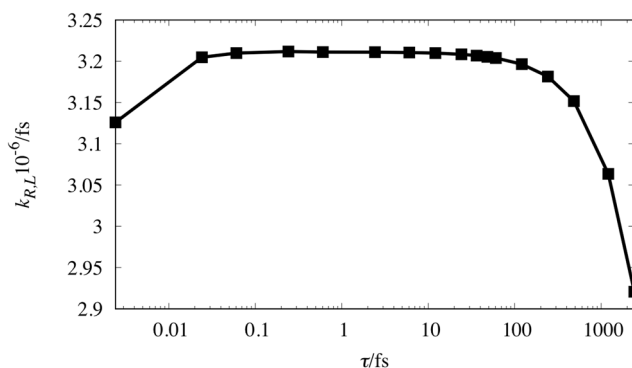
FIG. 14. Thermal barrier crossing as a function of τ for the highest coupling, $\lambda = 1.5\lambda_0$ case.

APPENDIX B: TRANSITION MATRIX DETAILS

Markov state models for TPT in the thermal case are assembled from $\tau = 250$ au (6.047 fs) density matrix calculations initialized in each eigenstate following Eq. (10). Max–min flux paths are determined with repeated applications of Dijkstra's algorithm.[81] A timescale (τ) that is too large risks incorporating large numbers of double jumps into the Markov model, thereby skipping over eigenstates in the reactive pathways. For the largest λ, the principal path length began to decrease, indicating double jumps becoming dominant, at approximately $\tau = 100$ fs. For the smallest λ, a change in the dominant path length did not occur until $\tau = 1000$ fs. A timescale that is too small leads to numerical problems due to off-diagonal entries in the transition matrix becoming negligible and diagonal entries becoming 1 to machine precision.

Figures 14 and 15 show the thermal barrier crossing rate as a function of τ for the largest and smallest λ in the study, respectively. Over many orders of magnitude in τ the rates remain stable. At very small τ, numerical issues result in instability, whereas the largest τ at high λ leads to instability by skipping steps along the reactive pathway. The chosen value of $\tau = 6.047$ fs is unlikely to result in the incorporation of double jumps while also avoiding potential numerical problems. The τ chosen was also verified by recalculating
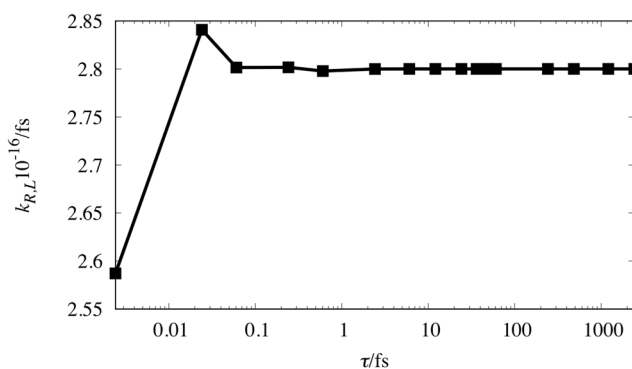
the Markov models at timescales an order of magnitude larger and smaller for the largest and smallest λ values and confirming that the thermal reaction rates, committors, and principal pathways were insensitive to the change.

REFERENCES

[1] B. Peters, *Reaction Rate Theory and Rare Events* (Elsevier, 2017).
[2] A. Nitzan, *Chemical Dynamics in Condensed Phases: Relaxation, Transfer and Reactions in Condensed Molecular Systems* (Oxford University Press, 2006).
[3] P. Hänggi, P. Talkner, and M. Borkovec, Rev. Mod. Phys. **62**, 251 (1990).
[4] W. H. Miller, J. Chem. Phys. **61**, 1823–1834 (1974).
[5] A. J. Leggett, Phys. Rev. B **30**, 1208 (1984).
[6] G. A. Voth, D. Chandler, and W. H. Miller, J. Chem. Phys. **91**, 7749–7760 (1989).
[7] J. C. Tully, J. Chem. Phys. **137**, 22A301 (2012).
[8] W. E and E. Vanden-Eijnden, Annu. Rev. Phys. Chem. **61**, 391–420 (2010).
[9] M. S. Schuurman and A. Stolow, Annu. Rev. Phys. Chem. **69**, 427–450 (2018).
[10] X. Zhu and D. R. Yarkony, Mol. Phys. **114**, 1983–2013 (2016).
[11] G. A. Worth and L. S. Cederbaum, Annu. Rev. Phys. Chem. **55**, 127–158 (2004).
[12] B. G. Levine and T. J. Martínez, Annu. Rev. Phys. Chem. **58**, 613–634 (2007).
[13] S. P. Neville, Y. Wang, A. E. Boguslavskiy, A. Stolow, and M. S. Schuurman, J. Chem. Phys. **144**, 014305 (2016).
[14] S. Matsika, J. Phys. Chem. A **109**, 7538–7545 (2005).
[15] B. F. E. Curchod and T. J. Martínez, Chem. Rev. **118**, 3305–3336 (2018).
[16] M. Barbatti, A. J. A. Aquino, J. J. Szymczak, D. Nachtigallová, P. Hobza, and H. Lischka, Proc. Natl. Acad. Sci. U. S. A. **107**, 21453–21458 (2010).
[17] T. Schultz, J. Quenneville, B. Levine, A. Toniolo, T. J. Martínez, S. Lochbrunner, M. Schmitt, J. P. Shaffer, M. Z. Zgierski, and A. Stolow, J. Am. Chem. Soc. **125**, 8098–8099 (2003).
[18] S. H. Courtney and G. R. Fleming, J. Chem. Phys. **83**, 215–222 (1985).
[19] J. M. Hicks, M. T. Vandersall, E. V. Sitzmann, and K. B. Eisenthal, Chem. Phys. Lett. **135**, 413–420 (1987).
[20] H. M. D. Bandara and S. C. Burdette, Chem. Soc. Rev. **41**, 1809–1825 (2012).
[21] A. J. Schile and D. T. Limmer, J. Chem. Phys. **151**, 014106 (2019).
[22] N. Y. Halpern and D. T. Limmer, Phys. Rev. A **101**, 042116 (2020).
[23] C. Chuang and P. Brumer, J. Phys. Chem. Lett. **12**, 3618–3624 (2021).
[24] D. G. Truhlar, B. C. Garrett, and S. J. Klippenstein, J. Phys. Chem. **100**, 12771–12800 (1996).
[25] T. J. H. Hele and S. C. Althorpe, J. Chem. Phys. **138**, 084108 (2013).
[26] T. J. H. Hele and S. C. Althorpe, J. Chem. Phys. **139**, 084116 (2013).
[27] P. G. Wolynes, Phys. Rev. Lett. **47**, 968–971 (1981).
[28] R. F. Grote and J. T. Hynes, J. Chem. Phys. **73**, 2715–2732 (1980).
[29] M. J. Gillan, Phys. Rev. Lett. **58**, 563–566 (1987).
[30] M. J. Gillan, J. Phys. C Solid State **20**, 3621–3641 (1987).
[31] G. A. Voth, J. Phys. Chem. **97**, 8365–8377 (1993).
[32] S. Jang and G. A. Voth, J. Chem. Phys. **112**, 8747–8757 (2000).
[33] S. Ranya and N. Ananth, J. Chem. Phys. **152**, 114112 (2020).
[34] T. J. H. Hele, M. J. Willatt, A. Muolo, and S. C. Althorpe, J. Chem. Phys. **142**, 191101 (2015).
[35] E. R. Heller and J. O. Richardson, J. Chem. Phys. **152**, 034106 (2020).
[36] J. E. Lawrence and D. E. Manolopoulos, J. Chem. Phys. **152**, 204117 (2020).
[37] S. Hammes-Schiffer, J. Am. Chem. Soc. **137**, 8860–8871 (2015).
[38] S. Hammes-Schiffer and J. C. Tully, J. Chem. Phys. **103**, 8528–8537 (1995).
[39] P. G. Wolynes, J. Chem. Phys. **87**, 6559–6561 (1987).
[40] Y. Litman, E. S. Pós, C. L. Box, R. Martinazzo, R. J. Maurer, and M. Rossi, J. Chem. Phys. **156**, 194107 (2022).
[41] J. S. Kretchmer and T. F. Miller III, J. Chem. Phys. **138**, 04B602 (2013).
[42] W. H. Miller, S. D. Schwartz, and J. W. Tromp, J. Chem. Phys. **79**, 4889–4898 (1983).
[43] X. Tao, P. Shushkov, and T. F. Miller, J. Chem. Phys. **148**, 102327 (2018).
[44] X. Tao, P. Shushkov, and T. F. Miller, J. Phys. Chem. A **123**, 3013–3020 (2019).

FIG. 15. Thermal barrier crossing rate as a function of τ for the lowest coupling, $\lambda = 0.05\lambda_0$ case.

[45] P. Shushkov, R. Li, and J. C. Tully, J. Chem. Phys. **137**, 22A549 (2012).

[46] J. E. Lawrence and D. E. Manolopoulos, J. Chem. Phys. **151**, 244109 (2019).

[47] J. O. Richardson and M. Thoss, J. Chem. Phys. **139**, 031102 (2013).

[48] W. Fang, M. J. Thapa, and J. O. Richardson, J. Chem. Phys. **151**, 214101 (2019).

[49] W. Fang, R. A. Zarotiadis, and J. O. Richardson, Phys. Chem. Chem. Phys. **22**, 10687–10698 (2020).

[50] J. E. Lawrence and D. E. Manolopoulos, J. Chem. Phys. **153**, 154113 (2020).

[51] B. Peters, Annu. Rev. Phys. Chem. **67**, 669–690 (2016).

[52] P. L. Geissler, C. Dellago, and D. Chandler, J. Phys. Chem. B **103**, 3706–3710 (1999).

[53] A. Dodin and A. P. Willard, J. Chem. Phys. **151**, 064106 (2019).

[54] A. Dodin, J. Provazza, D. F. Coker, and A. P. Willard, J. Chem. Theory Comput. **18**, 2047–2061 (2022).

[55] H. M. Wiseman and J. M. Gambetta, Phys. Rev. Lett. **101**, 140401 (2008).

[56] H. P. Breuer and F. Petruccione, *The Theory of Open Quantum Systems* (Oxford University Press on Demand, 2002).

[57] J. P. Garrahan and M. Guţă, Phys. Rev. A **98**, 052137 (2018).

[58] Z. K. Minev, S. O. Mundhada, S. Shankar, P. Reinhold, R. Gutiérrez-Jáuregui, R. J. Schoelkopf, M. Mirrahimi, H. J. Carmichael, and M. H. Devoret, Nature **570**, 200–204 (2019).

[59] F. Carollo, R. L. Jack, and J. P. Garrahan, Phys. Rev. Lett. **122**, 130605 (2019).

[60] F. Carollo, J. P. Garrahan, and R. L. Jack, J. Stat. Phys. **184**, 1572–9613 (2021).

[61] G. Perfetto, F. Carollo, and I. Lesanovsky, arXiv:2112.05078 (2021).

[62] A. J. Schile and D. T. Limmer, J. Chem. Phys. **149**, 214109 (2018).

[63] P. G. Bolhuis, D. Chandler, C. Dellago, and P. L. Geissler, Annu. Rev. Phys. Chem. **53**, 291–318 (2002).

[64] P. Metzner, C. Schütte, and E. Vanden-Eijnden, J. Chem. Phys. **125**, 084110 (2006).

[65] F. Noé, C. Schütte, E. Vanden-Eijnden, L. Reich, and T. R. Weikl, Proc. Natl. Acad. Sci. U. S. A. **106**, 19011–19016 (2009).

[66] Y. Meng, D. Shukla, V. S. Pande, and B. Roux, Proc. Natl. Acad. Sci. **113**, 9193–9198 (2016).

[67] T.-Q. Yu, M. Lapelosa, E. Vanden-Eijnden, and C. F. Abrams, J. Am. Chem. Soc. **137**, 3041–3050 (2015).

[68] W. Zheng, E. Gallicchio, N. Deng, M. Andrec, and R. M. Levy, J. Phys. Chem. B **115**, 1512–1523 (2011).

[69] H. Köppel, W. Domcke, and L. S. Cederbaum, Adv. Chem. Phys. **57**, 59–246 (1984).

[70] C. Dellago, P. G. Bolhuis, and D. Chandler, J. Chem. Phys. **110**, 6617–6625 (1999).

[71] S. C. Nguyen, J. P. Lomont, B. W. Caplins, and C. B. Harris, J. Phys. Chem. Lett. **5**, 2974–2978 (2014).

[72] W. T. Pollard and R. A. Friesner, J. Chem. Phys. **100**, 5054–5065 (1994).

[73] R. Alicki, D. A. Lidar, and P. Zanardi, Phys. Rev. A **73**, 052311 (2006).

[74] J. Jeske and J. H. Cole, Phys. Rev. A **87**, 052138 (2013).

[75] A. Levy, E. Rabani, and D. T. Limmer, Phys. Rev. Res. **3**, 023252 (2021).

[76] M. B. Plenio and P. L. Knight, Rev. Mod. Phys. **70**, 101 (1998).

[77] D. J. Wales, Annu. Rev. Phys. Chem. **69**, 401–425 (2018).

[78] D. J. Sharpe and D. J. Wales, J. Chem. Phys. **155**, 140901 (2021).

[79] L. Onsager, Phys. Rev. **54**, 554 (1938).

[80] J. D. Chodera and V. S. Pande, Phys. Rev. Lett. **107**, 098102 (2011).

[81] E. W. Dijkstra, Numer. Math. **1**, 269–271 (1959).

[82] L. Chen, M. F. Gelin, V. Y. Chernyak, W. Domcke, and Y. Zhao, Faraday Discuss. **194**, 61–80 (2016).

[83] J. Cao, C. Minichino, and G. A. Voth, J. Chem. Phys. **103**, 1391–1399 (1995).

[84] A. F. Izmaylov, D. Mendive-Tapia, M. J. Bearpark, M. A. Robb, J. C. Tully, and M. J. Frisch, J. Chem. Phys. **135**, 234106 (2011).

[85] I. G. Ryabinkin and A. F. Izmaylov, Phys. Rev. Lett. **111**, 220406 (2013).

[86] A. F. Izmaylov, J. Li, and L. Joubert-Doriol, J. Chem. Theory Comput. **12**, 5278–5283 (2016).

[87] W. G. Unruh, Phys. Rev. A **51**, 992–997 (1995).

[88] J. L. Skinner and D. Hsu, J. Phys. Chem. **90**, 4931–4938 (1986).

[89] J. H. Reina, L. Quiroga, and N. F. Johnson, Phys. Rev. A **65**, 032326 (2002).

[90] H. B. Chen, P. Y. Lo, C. Gneiting, J. Bae, Y. N. Chen, and F. Nori, Nat. Commun. **10**, 1–9 (2019).

[91] L.-M. Duan and G.-C. Guo, Phys. Rev. A **57**, 737–741 (1998).

[92] A. Seif, Y. X. Wang, and A. A. Clerk, Phys. Rev. Lett. **128**, 070402 (2022).

[93] M. Schlosshauer, Phys. Rep. **831**, 1–57 (2019).

[94] A. Naesby, T. Suhr, P. T. Kristensen, and J. Mørk, Phys. Rev. A **78**, 045802 (2008).

[95] M. Schlosshauer, A. P. Hines, and G. J. Milburn, Phys. Rev. A **77**, 022111 (2008).

[96] V. Ambegaokar, J. Stat. Phys. **125**, 1183–1192 (2006).

[97] C.-M. Goletz and F. Grossmann, J. Chem. Phys. **130**, 244107 (2009).

[98] S. Banerjee, Physica A **337**, 67–80 (2004).

[99] S.-J. Xiong, L. Chen, and Y. Zhao, Chem. Phys. Chem. **15**, 2859–2870 (2014).

[100] E. R. Heller, J. O. Joswig, and G. Seifert, Theor. Chem. Acc. **140**, 1432–2234 (2021).

[101] Z. Lan, L. M. Frutos, A. L. Sobolewski, and W. Domcke, Proc. Natl. Acad. Sci. U. S. A. **105**, 12707–12712 (2008).

[102] U. Manthe and H. Köppel, J. Chem. Phys. **93**, 1658–1669 (1990).

[103] M. C. Anderson, A. J. Schile, and D. T. Limmer (2022). "Nonadiabatic transition paths from quantum jump trajectories," Zenodo, v. 1.0. https://doi.org/10.5281/zenodo.6950371